

D-TENSORF: TENSORIAL RADIANCE FIELDS FOR DYNAMIC SCENES

Hankyu Jang & Daeyoung Kim

School of Computing

KAIST

Daejeon, South Korea

{gksrb97, kimd}@kaist.ac.kr

ABSTRACT

Neural radiance field (NeRF) attracts attention as a promising approach to reconstructing the 3D scene. As NeRF emerges, subsequent studies have been conducted to model dynamic scenes, which include motions or topological changes. However, most of them use an additional deformation network, slowing down the training and rendering speed. Tensorial radiance field (TensorRF) recently shows its potential for fast, high-quality reconstruction with compact model size by using multiple factorized components of an explicit data structure (4D tensor) and a small-sized neural network. Nonetheless, TensorRF is still only applicable to static scenes. In this paper, we present D-TensorRF, a tensorial radiance field for dynamic scenes, enabling novel view synthesis at a specific time. We consider the radiance field of a dynamic scene as a 5D tensor. The 5D tensor represents a 4D grid in which each axis corresponds to X, Y, Z, and time and has multi-channel features per element. Similar to TensorRF, we decompose the grid either into rank-one vector components (CP decomposition) or low-rank matrix components (MM decomposition). We newly propose matrix-matrix (MM) decomposition to reduce the amount of computation compared to CP decomposition and shorten the training time. We also use smoothing regularization to reflect the relationship between features at different times (temporal dependency). Through ablation study, we reveal that smoothing regularization is essential when modeling dynamic scenes. Above all, D-TensorRF with both CP and MM decomposition have significantly more compact model sizes than existing works. We show that D-TensorRF with CP decomposition and MM decomposition both have short training times and low memory footprints with quantitatively and qualitatively competitive rendering results in comparison to the state-of-the-art methods in 3D dynamic scene modeling.

1 INTRODUCTION

The reconstruction and modeling of 3D scenes play an essential role in various applications such as virtual reality, 3D visual content creation, and the film and game industry. Neural radiance fields (NeRF)(Mildenhall et al. (2021)) and recent subsequent research (Chen et al. (2022), Müller et al. (2022)) based on it achieve photo-realistic rendering.

Recently, methods using explicit data structures(Yu et al. (2021b), Hedman et al. (2021), Sun et al. (2021), Müller et al. (2022), Chen et al. (2022)) show faster training and rendering speeds. Tensorial radiance fields (TensorRF)(Chen et al. (2022)) accomplishes a fast training time by using a 3D feature grid and small-sized of a neural network simultaneously. TensorRF even decomposes the feature grid into low-rank tensor components to achieve a lower memory footprint than other methods using the explicit data structure.

Most NeRF methods focus on modeling static scenes rather than dynamic scenes with movement. However, the 3d reconstruction from the images of a moving object is much more applicable to various real-life applications. Especially, modeling a dynamic scene is also indispensable when considering the data collection process in real life. In the data collection process, an object is photographed simultaneously with a large number of cameras or photographed multiple times from

several directions with a small number of cameras. The latter option is commonly used due to affordable expenses. In this case, smoothly changing images are obtained according to the shooting time because many real-life cases include object motions or topological changes.

Including D-NeRF(Pumarola et al. (2020)), many studies(Park et al. (2021b), Tretschk et al. (2020), Li et al. (2021)) have been conducted recently to model a dynamic scene. Most studies use an additional deformation network that maps the coordinates of the sampled points to the canonical space. Since the deformation network is the same size as the radiance network that predicts color and density, it involves a longer training time and slower rendering speed.

Inspired by the idea of TensorRF, we represent the dynamic scene as a 5D tensor which represents a 4D grid in which each axis corresponds to X, Y, Z, and time. Moreover, each element of the 4D grid has a single-channel or multi-channel feature. Then, we applied tensor decomposition to the 4D grid.

We attempt the classic CANDECOMP/PARAFAC (CP) decomposition(Carroll & Chang (1970)) to factorize the 5D tensor first. Even with CP decomposition, we produce competitive rendering results compared to the state-of-the-art methods. Even though CP decomposition makes the model substantially compact, more components are required to model complex scenes, which increases computational cost and training time. To prevent this limitation, we propose a matrix-matrix (MM) decomposition that factorizes the full tensor of a radiance field into multiple matrix factors. Although the model size is slightly increased in contrast to when using the CP decomposition, the computational overhead is reduced significantly.

However, naively extending the time dimension of the TensorRF framework does not produce the desired result. This is because it does not consider the temporal dependency, which is the relation between the scenes at different times. According to our observation that the scenes at the adjacent times are closely related, we apply a smoothing regularization along the time axis to reflect the temporal dependency.

We conduct the experiments with our models (both with CP decomposition and MM decomposition) in various settings (different grid resolutions and the number of components). We show that our model’s rendering results are competitive compared to existing methods and demonstrate efficiency in terms of memory footprint and training speed. Our model with MM decomposition achieves satisfactory performance with only 8 minutes of training, and the model with CP decomposition requires only 1.8 MB. In addition, we carry out an ablation study on smoothing regularization to prove its importance.

To sum up, our main contributions are listed as follows:

- We express a dynamic scene with object motion or topological change from a tensorial perspective. We suggest a solution to model the dynamic scene by optimizing low-rank tensor components. We factorize the low-rank tensor components with the CP/MM decomposition and each component has factors related to the X, Y, Z, and time axes.
- We apply the smoothing regularization to the time-related factor of each low-rank tensor component to reflect the temporal dependency.
- Both our models with CP decomposition and MM decomposition achieve good rendering quality in both qualitative and quantitative terms. More importantly, our models are significantly compact and fast in training.

2 RELATED WORK

2.1 NEURAL RADIANCE FIELDS

Different kinds of 3D scene representations, such as meshes, point clouds, volumes, and implicit representations(Chen & Zhang (2018), Lombardi et al. (2019), Mildenhall et al. (2019), Munkberg et al. (2021), Park et al. (2019), Sitzmann et al. (2019), Tang et al. (2022a)), have been studied in order to improve rendering quality. To represent a 3D scene, NeRF(Mildenhall et al. (2021)) proposes to use a neural network as a function that receives position and viewing direction and outputs corresponding color and density. This representation achieves photo-realistic results and shows its

potential. It has been studied extensively and applied in various graphic or vision applications such as surface reconstruction(Oechsle et al. (2021)), fast rendering(Garbin et al. (2021), Reiser et al. (2021)), texture mapping(Baatz et al. (2021)), and dynamic scenes(Pumarola et al. (2020), Park et al. (2021b), Park et al. (2021a), Fang et al. (2022)).

Recent approaches to this representation can be categorized into implicit, explicit, and hybrid representations. The implicit representation, such as NeRF(Mildenhall et al. (2021)) is purely MLP-based. Even though the representation is straightforward, the high computation cost of MLP impedes training and rendering speed. The explicit representation is the method that tries to model a 3D scene with only explicit data structures storing features, not using a single neural network. Plenoxels(Yu et al. (2021a)) only uses a sparse 3D voxel grid with spherical harmonics and achieves desirable rendering quality. Although it is possible to reduce the expensive computation of MLP, the memory footprint is increased compared to the implicit representation. Hybrid representations use both an explicit data structure (sparse voxel grids(Liu et al. (2020)), octrees(Yu et al. (2021b)), multi-resolution hashmap(Müller et al. (2022)), low-rank tensor components(Chen et al. (2022))) and a small neural network. This lessens the size of the model and training time concurrently.

Several types of research to model the radiance field for dynamic scenes have also been conducted. One is to extend the time dimension in the radiance field for a static scene(Du et al. (2021), Gao et al. (2021), Pumarola et al. (2020)). Most approaches take advantage of the additional deformation field to predict motions(Pumarola et al. (2020), Park et al. (2021b), Fang et al. (2022)). The deformation field maps the point coordinates into the canonical space and passes them to the radiance network as inputs. To improve rendering quality, HyperNeRF(Park et al. (2021b)) uses hyperspace to reflect the discontinuity of the deformation field, and NR-NeRF(Tretschk et al. (2020)) segments a nonrigid foreground and a rigid background. However, the previous methods are based on implicit representations, which are very slow in training. Recently, TiNeuVox(Fang et al. (2022)) accelerates the training speed by using explicit voxel features with neural networks, including the deformation and radiance network.

Our model is a kind of hybrid representation. We utilize both an explicit 4D grid and a radiance network. Unlike the conventional methods, we do not use any other deformation network.

2.2 TENSOR DECOMPOSITION

Tensor decomposition is one of the effective methods for analyzing tensors, which are multi-dimensional arrays. Tensor decomposition of high-order tensors(Kolda & Bader (2009)) can be thought of as an extended, generalized version of matrix singular value decomposition. Various fields mainly use Tucker decomposition(Tucker (1966)) and CP decomposition(Carroll & Chang (1970)). Tucker decomposition factorizes a tensor into a core tensor multiplied by a matrix along each mode. CP decomposition is a particular case of Tucker decomposition in which a core tensor is restricted to being diagonal.

Tensor decomposition has been used in many fields, for example, anomaly detection(Kolda & Sun (2008)), recommender systems(Symeonidis & Zioupos (2016)), or multiple vision tasks(Ye et al. (2020), Lu et al. (2016)). TATD (Time Aware Tensor Decomposition)(Ahn et al. (2020)) is suggested to decompose temporal tensors for missing entry prediction by considering the characteristics of temporal tensors: temporal dependency and time-dependent sparsity.

In particular, TensorRF(Chen et al. (2022)) decomposes the neural radiance field using tensor decomposition(CP decomposition and vector-matrix decomposition (VM) for the first time. TensorRF, thereby, successfully reduces the training time and memory costs for storing features.

Moreover, CCNeRF(Tang et al. (2022b)) only uses pure tensor rank decomposition without using MLP. This method enables compression of the neural radiance field by maintaining low-rank approximation properties.

We consider the dynamic radiance field as a temporal tensor, including the time axis, and factorize it through tensor decomposition. Also, we apply the smoothing regularization for temporal dependency.

3 PRELIMINARY

3.1 NEURAL RADIANCE FIELDS

NeRF (Mildenhall et al. (2021)) is a representation of a 3D volumetric scene. This representation approximates the scene with a function $F_{\Theta} : (\mathbf{x}, \mathbf{d}) \rightarrow (\mathbf{c}, \sigma)$. The function is simply implemented with MLP. \mathbf{x} denotes 3d coordinates of points (x, y, z) and \mathbf{d} is 2d viewing direction (θ, ϕ) . Each \mathbf{c}, σ corresponds to emitted color and volume density. Given a camera ray \mathbf{r} whose origin is \mathbf{o} and direction is \mathbf{d} can be expressed as $\mathbf{r} = \mathbf{o} + t\mathbf{d}$ where t is distance from predefined range $[t_n, t_f]$. Points sampled along ray $\mathbf{x}_i = \mathbf{o} + t_i\mathbf{d}$ are taken as inputs of F_{Θ} . The function F_{Θ} outputs colors c_i and densities σ_i . The expected color of the pixel corresponding to the ray can be estimated by the quadrature rule:

$$\hat{\mathbf{C}}(r) = \sum_{i=1}^N T_i (1 - \exp(-\sigma_i \delta_i)) \mathbf{c}_i, T_i = \exp(-\sum_{j=1}^{i-1} \sigma_j \delta_j) \quad (1)$$

where $\delta_i = t_{i+1} - t_i$ is a distance between sampled points. Finally, NeRF is optimized with 2D images from different viewing directions by minimizing the following loss:

$$L = \left\| \hat{\mathbf{C}}(\mathbf{r}) - \mathbf{C}(\mathbf{r}) \right\|^2 \quad (2)$$

where $\mathbf{C}(\mathbf{r})$ is ground truth color of the pixel.

3.2 TENSORIAL RADIANCE FIELDS

The original NeRF (Mildenhall et al. (2021)) is computationally expensive because it uses 8 fully-connected layers. Therefore, many works tried to reduce the computational cost by adopting an explicit data structure. However, explicit data structure requires much memory to store features. Tensorial Radiance Fields (TensorRF)(Chen et al. (2022)) is proposed while pointing out these two limitations of existing methods.

TensorRF uses two 3D voxel grids to retain color-related features(multi-channel) or density-related features(single channel). After obtaining features according to the 3d location \mathbf{x} , the density-related feature values are used directly as volume density σ . The color-related feature vectors are converted into view-dependent color \mathbf{c} under the condition of the viewing direction \mathbf{d} through the pre-defined function S . This grid based-radiance field can be expressed as follows:

$$\sigma, c = \mathbf{G}_{\sigma}(\mathbf{x}), S(\mathbf{G}_c(\mathbf{x}), \mathbf{d}) \quad (3)$$

Geometry grid(density-related) is a 3D tensor $\mathbf{G}_{\sigma} \in \mathbb{R}^{I \times J \times K}$ and appearance grid(color-related) is a 4D tensor $\mathbf{G}_c \in \mathbb{R}^{I \times J \times K \times P}$. $I, J,$ and K correspond to the resolution of the feature grid along the $X, Y,$ and Z axes, respectively, and P is the number of feature channels.

TensorRF factorizes the geometry grid \mathbf{G}_{σ} and the appearance grid \mathbf{G}_c in two ways to make the model size compact. First, it directly applies the classic CP decomposition, which factorizes the tensor as a summation of rank-one tensor components, where each component is the outer product of the vector factors. With CP decomposition, Geometry grid \mathbf{G}_{σ} and appearance grid \mathbf{G}_c are decomposed as:

$$\mathbf{G}_{\sigma} = \sum_{r=1}^{R_{\sigma}} v_{\sigma,r}^X \circ v_{\sigma,r}^Y \circ v_{\sigma,r}^Z \quad (4)$$

$$\mathbf{G}_c = \sum_{r=1}^{R_c} v_{c,r}^X \circ v_{c,r}^Y \circ v_{c,r}^Z \circ b_r \quad (5)$$

v^X , v^Y , and v^Z denote the vector factors associated with X, Y and Z axis and b_r is an additional vector for feature channel dimension. Due to the high compactness of CP decomposition, it requires a large number of R_σ, R_c to model complex 3D scenes. This leads to an increase in the computational cost

Second, TensorRF proposes using Vector-Matrix (VM) decomposition, which factorizes the tensor into multiple vectors and matrices as follows:

$$\mathbf{G}_\sigma = \sum_{r=1}^{R_\sigma} v_{\sigma,r}^X \circ M_{\sigma,r}^{Y,Z} + v_{\sigma,r}^Y \circ M_{\sigma,r}^{X,Z} + v_{\sigma,r}^Z \circ M_{\sigma,r}^{X,Y} \quad (6)$$

$$\mathbf{G}_c = \sum_{r=1}^{R_c} v_{c,r}^X \circ M_{c,r}^{Y,Z} \circ b_{3r-2} + v_{c,r}^Y \circ M_{c,r}^{X,Z} \circ b_{3r-1} + v_{c,r}^Z \circ M_{c,r}^{X,Y} \circ b_{3r} \quad (7)$$

Matrix factors include information corresponding to two of the X, Y , and Z axes. Compared to using CP decomposition, TensorRF with VM decomposition requires more memory because matrices have more parameters than vectors. However, since matrices have much more information, TensorRF with VM decomposition achieves high rendering quality with only a small number of components, effectively reducing the computational cost. Finally, it renders images with a combination of Eqn.1, 3

4 METHOD

In section 4.1, 4.2, we explain how the dynamic radiance field is represented and factorized from a tensorial perspective. Then we describe how the smoothing regularization is applied in section 4.3. Finally, the implementation details are illustrated in section 4.5.

4.1 TENSORIAL RADIANCE FIELD REPRESENTATION FOR DYNAMIC SCENE

TensorRF utilizes multiple photos of a non-moving object, but the data we can easily obtain in the real world often involves movement over time. Our model aims to optimize the dynamic radiance field, which is a function F that maps 3D location $\mathbf{x} = (x, y, z)$, viewing direction $\mathbf{d} = (\theta, \phi)$ and time instant t to emitted color \mathbf{c} and volume density σ . This can be written as follows:

$$F : (\mathbf{x}, \mathbf{d}, t) \rightarrow (\mathbf{c}, \sigma) \quad (8)$$

Similar to TensorRF, we model the function F with 4D grids, 1) a geometry grid \mathbf{G}_σ and 2) a appearance grid \mathbf{G}_c . Each dimension of the 4D grid corresponds to the X, Y, Z , and time axis and stores features in each element of the grids. Our model outputs emitted color \mathbf{c} from the appearance feature and the viewing direction \mathbf{d} with an extra converting function S . We use the value of the geometry feature as volume density σ . This dynamic tensorial radiance field(D-TensorRF) can be rewritten as:

$$\sigma, \mathbf{c} = \mathbf{G}_\sigma(\mathbf{x}, t), S(\mathbf{G}_c(\mathbf{x}, t), \mathbf{d}) \quad (9)$$

$\mathbf{G}_\sigma(\mathbf{x}, t)$, $\mathbf{G}_c(\mathbf{x}, t)$ are quadrilinear interpolated features from the geometry grid and the appearance grid respectively at location \mathbf{x} and at time t . We can use both a small-sized MLP(2 fully-connected layers) and spherical harmonics as S , but MLP consistently shows better results.

4.2 FACTORIZING DYNAMIC RADIANCE FIELD

We approximate the geometry grid and the appearance grid $\mathbf{G}_\sigma, \mathbf{G}_c$ with factorized tensors (Fig. 1). The geometry grid is a 4D tensor $\mathbf{G}_\sigma \in \mathbb{R}^{I \times J \times K \times N}$ and the appearance grid is a 5D tensor $\mathbf{G}_c \in \mathbb{R}^{I \times J \times K \times N \times P}$. I, J, K , and N correspond to the resolution of the feature grid along the X, Y, Z , and time axes respectively, and P is the number of feature channels.

We decompose the dynamic radiance field with CP decomposition and Matrix-Matrix(MM) decomposition. Classic CP decomposition is directly applied to $\mathbf{G}_\sigma, \mathbf{G}_c$, and its decomposition equations are simply extended versions of Eqn.4, 5 with an additional vector corresponding to the time axis.

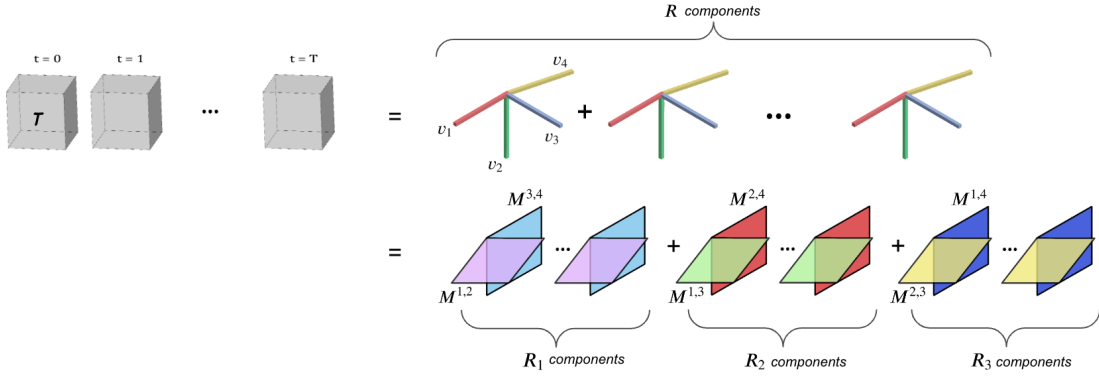


Figure 1: Tensor decomposition of 4D tensor. While CP decomposition factorizes the 4D tensor into a summation of outer products of vector factors, MM decomposition factorizes the tensor into a summation of outer products of matrix factors(Eqn.10).

To reduce the number of components required to model a scene, we newly propose Matrix-Matrix(MM) decomposition, which only utilizes matrix factors. Given a 4D tensor $\mathbf{T} \in \mathbb{R}^{I \times J \times K \times N}$, MM decomposition can be expressed as:

$$\mathbf{T} = \sum_{r=1}^{R_1} M_r^{1,2} \circ M_r^{3,4} + \sum_{r=1}^{R_2} M_r^{1,3} \circ M_r^{2,4} + \sum_{r=1}^{R_3} M_r^{2,3} \circ M_r^{1,4} \quad (10)$$

$$\text{where } M_r^{1,2} \in \mathbb{R}^{I \times J}, M_r^{1,3} \in \mathbb{R}^{I \times K}, M_r^{1,4} \in \mathbb{R}^{I \times N}, \\ M_r^{2,3} \in \mathbb{R}^{J \times K}, M_r^{2,4} \in \mathbb{R}^{J \times N}, M_r^{3,4} \in \mathbb{R}^{K \times N}$$

Each matrix corresponds to two modes of four modes (X, Y, Z , and time axes). While CP decomposition represents every mode with separate vectors, we combine every two modes and represent them by matrices. Even though this relaxes the compactness of the model, it can express complex scenes with a smaller number of components compared to CP decomposition. Still memory complexity is decreased from $O(n^4)$ to $O(n^2)$ compared to naive 4D grid representation.

With MM decomposition, the 4D geometry grid and the 5D appearance grid $\mathbf{G}_\sigma, \mathbf{G}_c$ are factorized as follows:

$$\mathbf{G}_\sigma = \sum_{r=1}^{R_\sigma} M_{\sigma,r}^{X,Y} \circ M_{\sigma,r}^{Z,T} + M_{\sigma,r}^{X,Z} \circ M_{\sigma,r}^{Y,T} + M_{\sigma,r}^{Y,Z} \circ M_{\sigma,r}^{X,T} \quad (11)$$

$$\mathbf{G}_c = \sum_{r=1}^{R_c} M_{c,r}^{X,Y} \circ M_{c,r}^{Z,T} \circ b_{3r-2} + M_{c,r}^{X,Z} \circ M_{c,r}^{Y,T} \circ b_{3r-1} + M_{c,r}^{Y,Z} \circ M_{c,r}^{X,T} \circ b_{3r} \quad (12)$$

With MM decomposition, the dynamic tensorial radiance field is factorized into $6R_c + 6R_\sigma$ matrices and $3R_c$ vectors. We choose the value of $6R_c, 6R_\sigma$ smaller than any of $I \times J, I \times K, I \times N, J \times K, J \times N, N \times K$ which leads our representation still compact.

4.3 SMOOTHING REGULARIZATION

Simply extending the time dimension is not enough to produce a satisfactory result, and it is shown in Fig.6. We must consider temporal dependency, which is the relation between the features at different

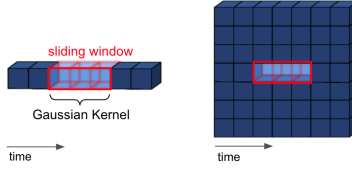


Figure 2: Smoothing regularization for models with CP decomposition(Left, Eqn.13) and MM decomposition(Right, Eqn.14). Smoothing regularization is applied while moving the predefined size of the window along the vector factor or the specific mode of matrix factor corresponding to the time axis.

times. We exploit the observation when the scene moves continuously over time; the appearance at t is most similar to that at $t-1$ and $t+1$. This means the features in the 4D grid should also be most close to those adjacent along the time axis.

To reflect temporal dependency, we introduce the regularization term(Eqn.13, 14). We apply the regularization along time-related factors for both our models with CP decomposition and MM decomposition(Fig .2).

$$L_{smooth} = \sum_{r=1}^R \sum_{v \in [v_r^T]} \sum_{i_t=0}^N \left\| e_{i_t}^v - \sum_{i_w \in window(i_t, S)} w(i_t, i_w) e_{i_w}^v \right\|^2 \quad (13)$$

$$L_{smooth} = \sum_{r=1}^R \sum_{m \in [M_r^{X,T}, M_r^{Y,T}, M_r^{Z,T}]} \sum_{l=0}^L \sum_{i_t=0}^N \left\| e_{l, i_t}^m - \sum_{i_w \in window(i_t, S)} w(i_t, i_w) e_{l, i_w}^m \right\|^2 \quad (14)$$

R is the value of R_σ or R_c , which is the number of low-rank tensor components of the geometry grid or the appearance grid. N is the resolution of the feature grid along the time axis, and L indicates the resolution of other axes. i_w denotes index which is close to i_t in a $window(i_t, S)$ of size S . $w(i_t, i_w)$ is utilized to force some dependency between features at adjacent times. Inspired by TATD(Ahn et al. (2020)), we choose the Gaussian kernel for the weight function $w(i_t, i_w)$ to reflect our observation that closer features along the time axis are more similar. The Gaussian kernel can be written as,

$$w(i_t, i_w) = \frac{K(i_t, i_w)}{\sum_{i'_w \in window(i_t, S)} K(i_t, i'_w)}, K(i_t, i_w) = exp(-(i_t - i_w)^2 / 2\sigma^2) \quad (15)$$

Where σ denotes the degree of smoothing. We used window size $S = 3$ and $\sigma = 0.5$ for our experiments. The Gaussian kernel has an additional advantage that it does not have any parameters to optimize, so our model can concentrate on learning the decomposed factors.

4.4 OVERALL FRAMEWORK

Our dynamic tensorial radiance field can be rewritten as:

$$\begin{aligned} \sigma &= \mathbf{G}_\sigma(\mathbf{x}, t) \\ &= \sum_{r=1}^{R_\sigma} M_{\sigma,r}^{X,Y}(x, y) \circ M_{\sigma,r}^{Z,T}(z, t) + M_{\sigma,r}^{X,Z}(x, z) \circ M_{\sigma,r}^{Y,T}(y, t) + M_{\sigma,r}^{Y,Z}(y, z) \circ M_{\sigma,r}^{X,T}(x, t) \end{aligned} \quad (16)$$

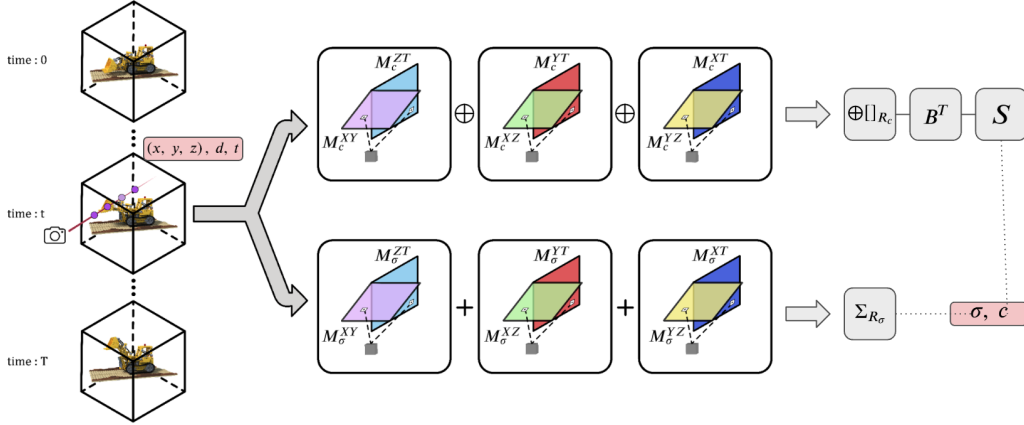


Figure 3: Overall framework of D-TensorRF with MM decomposition.

$$\begin{aligned}
\mathbf{c} &= \mathbf{G}_c(\mathbf{x}, t) \\
&= \sum_{r=1}^{R_c} M_{c,r}^{X,Y}(x, y) \circ M_{c,r}^{Z,T}(z, t) \circ b_{3r-2} \\
&\quad + M_{c,r}^{X,Z}(x, z) \circ M_{c,r}^{Y,T}(y, t) \circ b_{3r-1} + M_{\sigma,r}^{Y,Z}(y, z) \circ M_{c,r}^{X,T}(x, t) \circ b_{3r} \\
&= \mathbf{B}(\oplus[(M_{c,r}^{X,Y}(x, y) \circ M_{c,r}^{Z,T}(z, t)) \\
&\quad \oplus (M_{c,r}^{X,Z}(x, z) \circ M_{c,r}^{Y,T}(y, t)) \oplus (M_{\sigma,r}^{Y,Z}(y, z) \circ M_{c,r}^{X,T}(x, t))]_{r=1, \dots, R_c})
\end{aligned} \tag{17}$$

Matrix B is constructed by stacking all b_r vectors. \oplus is the concatenation operator, and it piles up all scalar values, which is a result of multiplying values from two matrices. Stacked scalar values construct a vector whose dimension is $3R_c$. After we obtain volume density σ and view-dependent color \mathbf{c} , we use differentiable volume rendering of NeRF(Eqn. 1) to render images.

Finally, we optimize our D-TensorRF by minimizing L2 rendering loss with 2D image supervision similar to Eqn. 2 via gradient descent. We utilize smoothing regularization to reflect temporal dependency. We also use an L1 regularization on our vector and matrix factors to prevent overfitting.

4.5 IMPLEMENTATION DETAILS

We implement our model based on the official implementation of TensorRF(Chen et al. (2022)). We use the appearance feature converting function S as a small MLP, which consists of two fully-connected layers with 128-channel hidden layers. SH function also works as a function S , but the performance is slightly lower than the MLP, shown in Tab. 1. Thus, we mostly choose to use the MLP.

The number of components for the appearance grid R_c is set to 3 times those for the geometry grid R_σ . We use the value of $N_t = 0.25 \times (\text{number of training images})$ as the dimension of the feature grid along the time axis. We upsample the vector and matrix factors linearly and bilinearly at training steps 2000, 3000, 4000, 5500, and 7000. We set the initial resolution of the feature grid as $64^3 \times N_t$. We do not upsample the feature grid along time axes.

In addition, we utilize a binary occupancy mask grid calculated at training step 2000 to make a more accurate bounding box that prevents unnecessary computation and precise modeling. We train D-TensorRF using a single GeForce RTX 3090 GPU. For other configurations, such as optimizer, learning rate, or batch size, we stick to the detail of the original TensorRF implementation.

5 EXPERIMENTS

5.1 EXPERIMENTS SETUP

We evaluate D-TensoRF on the extended Synthetic Nerf dataset provided by D-NeRF (Pumarola et al. (2020)). The dataset consists of eight scenes which include the motions of the objects. Each scene has 50 \sim 200 training images and 20 test images. Images of each scene are obtained at different times. We train images at 400×400 pixels.

We also train TensorRF models with CP and VM decomposition for comparison with D-TensoRF models. We define the number of voxels in the feature grid of 64^3 at the beginning of training. The number of final voxels is 150^3 for TensorRF CP decomposition and 100^3 for TensorRF-VM decomposition.

We conduct a quantitative and qualitative evaluation with various existing methods. NeRF (Mildenhall et al. (2021)), DirectVoxGo (Sun et al. (2021)), Plenoxels (Yu et al. (2021a)), and TensorRF (Chen et al. (2022)) are the methods for reconstructing 3D static scenes. DirectVoxGo, Plenoxels, and TensorRF use explicit data structures to accelerate the training speed. We compare our D-TensoRFs with these methods to show that ours are suitable to model dynamic scenes. T-NeRF (Pumarola et al. (2020)), D-NeRF (Pumarola et al. (2020)), TiNeuVox-S (Fang et al. (2022)), and TiNeuVox-B (Fang et al. (2022)) are targeted to dynamic scenes. T-NeRF directly gives time information by extending an additional input dimension to the radiance field. D-Nerf, TiNeuVox-S, and TiNeuVox-B use an additional deformation field. Especially, TiNeuVox-S and TiNeuVox-B take advantage of time-aware neural voxels to reduce the training time.

We use three evaluation metrics; Peak signal-to-noise ratio (PSNR), structural similarity (SSIM) (Wang et al. (2004)), and learned perceptual image patch similarity (LPIPS)(Zhang et al. (2018)). PSNR is the ratio between the maximum possible value of a signal and the power of distorting noise. For our experiments, It is defined by the maximum possible pixel value of the image and the mean squared error(MSE) between the rendered result and the ground truth. When PSNR is high, MSE is small, and the image is high-quality. SSIM measures the similarity between two images. SSIM is calculated in terms of luminance, contrast, and structure. The image is considered to be similar to the ground truth when the SSIM score is high. LPIPS estimates the perceptual similarity between two images. It evaluates the distance between images using the features extracted from the pre-trained deep network. Lower LPIPS means more perceptually similar.

In addition, we present an analysis of D-TensoRF models with different numbers of components and different numbers of voxels (the grid resolution). An ablation study is conducted on smoothing regularization to verify the importance of reflecting temporal dependency.

5.2 QUANTITATIVE EVALUATION

In Tab. 1, we show the quantitative results of D-TensoRF-CP, D-TensoRF-MM, and the existing methods. As NeRF and TensorRF aim at modeling static scenes, it is shown that they do not correctly model dynamic scenes in all evaluation metrics.

T-NeRF, a NeRF method for modeling dynamic scenes, can be considered to be a similar approach to ours, but D-TensoRF-CP and D-TensoRF-MM outperformed T-Nerf in all evaluation metrics. D-Nerf, TiNeuVox-S, and TiNeuVox-B are the methods that use an deformation network and show good evaluation scores. Compared to them, D-TensoRF-CP or D-TensoRF-MM have slightly lower PSNR scores, but SSIM and LPIPS show almost similar or better scores. Our models consistently stand out in the LPIPS evaluation metric, although the PSNR score is slightly lower than the best score.

We also report the per-scene quantitative comparisons in Tab.5. D-TensoRF-CP and D-TensoRF-MM show satisfactory LPIPS scores in all scenes. In particular, in scenes where the motion between images at adjacent times is not very large, ours have better PSNR and SSIM scores than baseline methods.

Regarding training speed, because T-Nerf and D-Nerf use only MLP purely, they are very slow (about 20 hours), whereas TiNeuVox shows a faster speed by utilizing explicit data structure. In particular, the TiNeuVox-S model shows promising results with an 8-minute training speed. Our

Table 1: Evaluation scores of baseline methods are taken from their papers whenever available. Training time is estimated on a single RTX 3090 GPU.

Method	Time↓	Size(MB)↓	PSNR↑	SSIM↑	LPIPS↓
NeRF (Mildenhall et al. (2021))	~hours	5	19.00	0.87	0.18
DirectVoxGo (Sun et al. (2021))	5 mins	205	18.61	0.85	0.17
Plenoxels (Yu et al. (2021a))	6 mins	717	20.24	0.87	0.16
TensoRF-CP384 (Chen et al. (2022))	14 mins	1	19.82	0.89	0.17
TensoRF-VM192 (Chen et al. (2022))	9 mins	8	19.68	0.88	0.17
T-NeRF (Pumarola et al. (2020))	~hours	-	29.51	0.96	0.08
D-NeRF (Pumarola et al. (2020))	20 hours	4	30.50	0.95	0.07
TiNeuVox-S (Fang et al. (2022))	8 mins	8	30.75	0.96	0.07
TiNeuVox-B (Fang et al. (2022))	28mins	48	32.67	0.97	0.04
Ours-CP768 ($150^3 \times N_t$, 60k steps)	39 mins	1.8	30.68	0.96	0.03
Ours-MM192 ($100^3 \times N_t$, 30k steps)	8 mins	10.8	29.74	0.96	0.04
Ours-MM192 ($100^3 \times N_t$, 60k steps)	16 mins	10.8	29.94	0.96	0.03
Ours-CP768-SH ($150^3 \times N_t$, 60k steps)	42 mins	1.6	29.52	0.95	0.04
Ours-MM192-SH ($100^3 \times N_t$, 60k steps)	16 mins	10.6	27.7	0.94	0.06

D-TensoRF-MM with 30k iterations obtains a better LPIPS score with the same 8-minute training speed. We can improve further by training up to 60k iterations, which took 16 minutes. D-TensoRF-CP takes a longer training time than D-TensoRF-MM at 39 minutes, but still, we can produce high evaluation scores in a training time of less than 1 hour.

Our model requires a significantly smaller memory footprint than all previous methods modeling dynamic scenes. The most compact model among previous methods, D-NeRF, required 4MB, but our D-TensoRF-CP required only 1.8MB, even though we used an explicit feature grid for fast training speed. D-TensoRF-MM requires 10.8 MB, slightly larger than the TiNeuVox-S and much more compact than TiNeuVox-B.

We also use the SH function to convert features into color and density, but it shows lower scores in all evaluation metrics compared to when the MLP is used. Still, LPIPS scores are similar to those of D-NeRF and TiNeuVox-S.

5.2.1 REVISITING PSNR SCORE



Figure 4: Additional rendering results of D-TensoRF with CP decomposition(Left) and MM decomposition(Right). D-TensoRF-CP tends to produce blurry results compared to D-TensoRF-MM.

We can observe that PSNR prefers blurry images to sharp images in Fig. 4, 5.3. In Fig. 4, even the rendering result of D-TensoRF-MM produces sharper images than D-TensoRF-CP, but the PSNR score is slightly lower. This is because PSNR is calculated based on pixel-level mean square error, so it is too sensitive to small shifts. Therefore, it cannot guarantee that the rendering quality of a model with a high PSNR score is satisfactory for human eyes. This phenomenon is also pointed out by Park et al. (2021b).

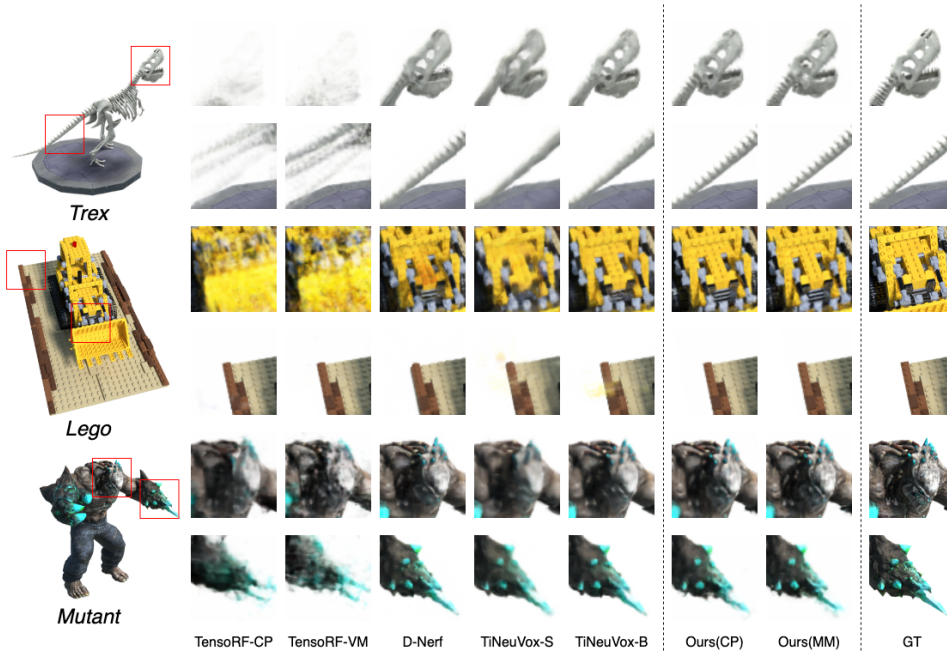


Figure 5: Qualitative results of D-TensorRF-CP, D-TensorRF-MM and baseline methods on the extended Synthetic NeRF scenes provided by D-NeRF(Pumarola et al. (2020)).

5.3 QUALITATIVE EVALUATION

We provide qualitative results of D-TensorRF-CP, D-TensorRF-MM, and the comparison methods in Fig.5.3. The two decomposition methods of TensorRF fail to model a dynamic scene. In particular, since the movement is not reflected at all, they give results that seem to indicate that some training images overlapped.

D-NeRF, Tineuvox-s, and Tineuvox-B appear to predict motion well. However, there is a problem of misprediction, which is a disadvantage of using a deformation network. In the Lego rendering results, D-NeRF shows an unrelated brown color where it should be yellow. Moreover, yellow appears where nothing should be in the results of Tineuvox-S and Tineuvox-B. Our methods, D-TensorRF-CP and D-TensorR-MM, do not have a misprediction problem because we do not use a deformation network.

Also, the overall results of the existing methods are blurred. In the rendered images of the T-rex, Tineuvox-S and Tineuvox-B can not express the pointy part. D-NeRF shows a sharper image than Tineuvox-S and Tineuvox-B, but the image is still more blurred than the results of D-TensorRF-CP and D-TensorRF-MM.

Our methods produce the sharpest image when there is a smooth motion. However, in the case of the mutant’s hand, the rendering result seems to be smudged compared to the ground truth. The result is similar to Tineuvox-B and Tineuvox-S and a little more smudged than D-NeRF. We presume this is because the smoothing regularization using the Gaussian kernel cannot perfectly model the temporal dependency when there is a large motion between the scenes in adjacent times.

We further demonstrate that D-TensorRF-CP and D-TensorRF-MM synthesize high-quality images of every scene at different times and unseen viewing directions in Fig. 8, 9, 10, and 11.

5.4 ANALYSIS OF DIFFERENT D-TENSORRF MODELS

We conduct an extensive evaluation while doubling the number of components from 192 to 768 for D-TensorRF-CP and doubling the number of components from 96 to 384 for D-TensorRF-MM.

Table 2: Evaluation scores of D-TensoRF-CP and D-TensoRF-MM with different number of components and final voxels.

	#Comp	$64^3 \times N_t$			$100^3 \times N_t$			$150^3 \times N_t$		
		PSNR \uparrow	SSIM \uparrow	LPIPS \downarrow	PSNR \uparrow	SSIM \uparrow	LPIPS \downarrow	PSNR \uparrow	SSIM \uparrow	LPIPS \downarrow
D-TensoRF-CP	192	16.38	0.883	0.241	16.45	0.884	0.243	16.46	0.885	0.241
	384	28.95	0.951	0.052	29.06	0.950	0.046	29.00	0.953	0.045
	768	30.41	0.961	0.038	29.64	0.963	0.033	30.68	0.963	0.031
D-TensoRF-MM	96	29.63	0.956	0.043	29.55	0.958	0.040	29.26	0.954	0.043
	192	29.97	0.961	0.035	29.94	0.960	0.034	29.71	0.958	0.034
	384	29.88	0.963	0.030	29.93	0.963	0.030	29.66	0.960	0.031

Table 3: Comparison of training speed and memory footprint in various settings. Training speed and memory footprint increases while the number of components and voxels increases.

	#Comp	$64^3 \times N_t$		$100^3 \times N_t$		$150^3 \times N_t$	
		Time \downarrow	Size(MB) \downarrow	Time \downarrow	Size(MB) \downarrow	Time \downarrow	Size(MB) \downarrow
D-TensoRF-CP	192	19:26	0.35	24:24	0.44	31:50	0.55
	384	18:10	0.58	20:58	0.74	26:51	0.99
	768	23:34	0.95	29:52	1.26	38:40	1.75
D-TensoRF-MM	96	14:46	2.64	15:42	5.46	18:21	11.13
	192	15:01	5.14	15:55	10.83	19:53	22.21
	384	15:39	10.10	16:58	21.33	23:15	43.89

Furthermore, we perform experiments when the number of final voxels is $64^3 \times N_t$, $100^3 \times N_t$, and $150^3 \times N_t$. In Tab.2, we show the qualitative comparisons between different D-TensoRFs.

In the case of D-TensoRF-CP, 192 components are not enough to model a dynamic scene. This is because only a little information can be contained per component due to the high compactness of the CP decomposition. The modeling performance comes out well when more than 384 components are used. D-TensoRF-MM shows high-quality results even with 96 components. The performances of both D-TensoRF-CP and D-TensoRF-MM tend to improve as the number of components grows.

However, the evaluation scores do not improve as the number of voxels increases. The number of points according to the coordinate (\mathbf{x}, t) included in one voxel of the feature grid increases when the grid resolution is too small. Thus, much information is compressed into one feature while optimizing the feature grid. As the expressiveness of the model reduces, the synthesized image is not sharp as a result. On the other hand, when the number of voxels is too large, only a few points corresponding to the coordinate (\mathbf{x}, t) are included in one voxel. The feature of non-moving parts acquires additional information from the features in adjacent times through smoothing regularization. However, the feature corresponding to moving parts even cannot obtain sufficient information from the features in adjacent times. Consequently, while the model with superabundant voxels can express non-moving parts in detail, the model renders a smudged image of moving parts.

In Fig.7, we show the rendered results when the number of voxels is $64^3 \times N_t$ and $150^3 \times N_t$. The synthesized images are blurry with $64^3 \times N_t$ voxels. The results with $150^3 \times N_t$ voxels can express the details sharp, but some appear to be smudged. We, therefore, select $150^3 \times N_t$ for D-TensoRF-CP, $100^3 \times N_t$ for D-TensoRF-MM as the number of final voxels which achieves the best rendering quality.

5.5 ABLATION STUDY ON SMOOTHING REGULARIZATION

An ablation study on smoothing regularization is also conducted. In Tab.4, evaluation metric scores increased by applying smoothing regularization. In Fig. 6, it can be seen that the quality significantly increases when the temporal dependency is reflected through smoothing regularization.

6 LIMITATIONS AND FUTURE WORK

We use a smoothing regularization using a Gaussian kernel based on the observation that the scene at time t most closely resembles the scenes at $t - 1$, $t + 1$. However, as shown in section 5.3, it fails



Figure 6: Ablation study on smoothing regularization in terms of rendering quality. The above images are the results when we apply the smoothing regularization. The below images are the results of not applying the smoothing regularization.

Table 4: Ablation study on smoothing regularization in terms of evaluation scores.

Method	PSNR \uparrow	SSIM \uparrow	LPIPS \downarrow
D-TensoRF-CP768($150^3 \times N_t$, w/o smoothing regularization)	28.91	0.95	0.04
D-TensoRF-CP768($150^3 \times N_t$, w smoothing regularization)	30.68	0.96	0.03
D-TensoRF-MM192($100^3 \times N_t$, w/o smoothing regularization)	27.72	0.95	0.04
D-TensoRF-MM192($100^3 \times N_t$, w smoothing regularization)	29.94	0.96	0.03

if there are large movements between adjacent scenes in the training dataset. Including these cases, our method could be further developed by applying a weight function other than the Gaussian kernel that more accurately reflects temporal dependencies.

Also, D-TensoRF can be applied only to bounded scenes similar to TensoRF. We suggest modeling the background and objects with motion separately can be the one way to resolve this limitation. Or, other approaches could possibly enable our methods to apply to unbounded scenes, we leave this as future work.

7 CONCLUSION

We present a method for synthesizing a high-quality scene in a novel time and viewing direction by modeling a dynamic scene. We decompose the dynamic radiance field into low-rank tensor components using the classic CP decomposition, and the newly proposed MM decomposition. Through this, the training time could be significantly reduced, as could the required memory footprint compared to existing methods.

In addition, by reflecting the temporal dependency, the motion is implicitly modeled using smoothing regularization. As a result, we can model the dynamic scene efficiently without using a deformation network.

D-TensoRF with CP decomposition and MM decomposition obtains competitive scores in all evaluation metrics. Especially, we achieve the state-of-the-art LPIPS scores, which reflects the perceptual quality. Our method have sharper images compared to existing methods in terms of quality. In addition, our method simultaneously achieve fast training time and a small memory footprint.

Based on 60k training steps, the training time is significantly reduced to 40 minutes for D-TensorRF with CP decomposition and to 16 minutes for MM decomposition. Also, the memory footprint is highly compact at 1.8MB for CP decomposition and at 10.8MB for MM decomposition.

REFERENCES

- Dawon Ahn, Jun-Gi Jang, and U Kang. Time-aware tensor decomposition for missing entry prediction. *CoRR*, abs/2012.08855, 2020. URL <https://arxiv.org/abs/2012.08855>.
- Hendrik Baatz, Jonathan Granskog, Marios Papas, Fabrice Rousselle, and Jan Novák. Nerf-tex: Neural reflectance field textures. In *Eurographics Symposium on Rendering*. The Eurographics Association, June 2021.
- J. Douglas Carroll and Jih-Jie Chang. Analysis of individual differences in multidimensional scaling via an n-way generalization of “eckart-young” decomposition. *Psychometrika*, 35(3):283–319, Sep 1970. ISSN 1860-0980. doi: 10.1007/BF02310791. URL <https://doi.org/10.1007/BF02310791>.
- Anpei Chen, Zexiang Xu, Andreas Geiger, Jingyi Yu, and Hao Su. Tensorf: Tensorial radiance fields, 2022. URL <https://arxiv.org/abs/2203.09517>.
- Zhiqin Chen and Hao Zhang. Learning implicit fields for generative shape modeling. *CoRR*, abs/1812.02822, 2018. URL <http://arxiv.org/abs/1812.02822>.
- Yilun Du, Yanan Zhang, Hong-Xing Yu, Joshua B. Tenenbaum, and Jiajun Wu. Neural radiance flow for 4d view synthesis and video processing. In *Proceedings of the IEEE/CVF International Conference on Computer Vision*, 2021.
- Jiemin Fang, Taoran Yi, Xinggang Wang, Lingxi Xie, Xiaopeng Zhang, Wenyu Liu, Matthias Nießner, and Qi Tian. Fast dynamic radiance fields with time-aware neural voxels. *arxiv:2205.15285*, 2022.
- Chen Gao, Ayush Saraf, Johannes Kopf, and Jia-Bin Huang. Dynamic view synthesis from dynamic monocular video. *CoRR*, abs/2105.06468, 2021. URL <https://arxiv.org/abs/2105.06468>.
- Stephan J. Garbin, Marek Kowalski, Matthew Johnson, Jamie Shotton, and Julien P. C. Valentin. Fastnerf: High-fidelity neural rendering at 200fps. *CoRR*, abs/2103.10380, 2021. URL <https://arxiv.org/abs/2103.10380>.
- Peter Hedman, Pratul P. Srinivasan, Ben Mildenhall, Jonathan T. Barron, and Paul E. Debevec. Baking neural radiance fields for real-time view synthesis. *CoRR*, abs/2103.14645, 2021. URL <https://arxiv.org/abs/2103.14645>.
- Tamara G. Kolda and Brett W. Bader. Tensor decompositions and applications. *SIAM Review*, 51(3):455–500, 2009. doi: 10.1137/07070111X. URL <https://doi.org/10.1137/07070111X>.
- Tamara G. Kolda and Jimeng Sun. Scalable tensor decompositions for multi-aspect data mining. In *2008 Eighth IEEE International Conference on Data Mining*, pp. 363–372, 2008. doi: 10.1109/ICDM.2008.89.
- Zhengqi Li, Simon Niklaus, Noah Snavely, and Oliver Wang. Neural scene flow fields for space-time view synthesis of dynamic scenes. In *Proceedings of the IEEE/CVF Conference on Computer Vision and Pattern Recognition (CVPR)*, 2021.
- Lingjie Liu, Jiatao Gu, Kyaw Zaw Lin, Tat-Seng Chua, and Christian Theobalt. Neural sparse voxel fields. *NeurIPS*, 2020.
- Stephen Lombardi, Tomas Simon, Jason Saragih, Gabriel Schwartz, Andreas Lehrmann, and Yaser Sheikh. Neural volumes: Learning dynamic renderable volumes from images. *ACM Trans. Graph.*, 38(4):65:1–65:14, July 2019.

-
- Zhiyun Lu, Vikas Sindhwani, and Tara N. Sainath. Learning compact recurrent neural networks. *CoRR*, abs/1604.02594, 2016. URL <http://arxiv.org/abs/1604.02594>.
- Ben Mildenhall, Pratul P. Srinivasan, Rodrigo Ortiz-Cayon, Nima Khademi Kalantari, Ravi Ramamoorthi, Ren Ng, and Abhishek Kar. Local light field fusion: Practical view synthesis with prescriptive sampling guidelines. *ACM Transactions on Graphics (TOG)*, 2019.
- Ben Mildenhall, Pratul P Srinivasan, Matthew Tancik, Jonathan T Barron, Ravi Ramamoorthi, and Ren Ng. Nerf: Representing scenes as neural radiance fields for view synthesis. *Communications of the ACM*, 65(1):99–106, 2021.
- Thomas Müller, Alex Evans, Christoph Schied, and Alexander Keller. Instant neural graphics primitives with a multiresolution hash encoding. *ACM Trans. Graph.*, 41(4):102:1–102:15, July 2022. doi: 10.1145/3528223.3530127. URL <https://doi.org/10.1145/3528223.3530127>.
- Jacob Munkberg, Jon Hasselgren, Tianchang Shen, Jun Gao, Wenzheng Chen, Alex Evans, Thomas Müller, and Sanja Fidler. Extracting triangular 3d models, materials, and lighting from images. *CoRR*, abs/2111.12503, 2021. URL <https://arxiv.org/abs/2111.12503>.
- Michael Oechsle, Songyou Peng, and Andreas Geiger. UNISURF: unifying neural implicit surfaces and radiance fields for multi-view reconstruction. *CoRR*, abs/2104.10078, 2021. URL <https://arxiv.org/abs/2104.10078>.
- Jeong Joon Park, Peter Florence, Julian Straub, Richard A. Newcombe, and Steven Lovegrove. DeepSDF: Learning continuous signed distance functions for shape representation. *CoRR*, abs/1901.05103, 2019. URL <http://arxiv.org/abs/1901.05103>.
- Keunhong Park, Utkarsh Sinha, Jonathan T. Barron, Sofien Bouaziz, Dan B Goldman, Steven M. Seitz, and Ricardo Martin-Brualla. Nerfies: Deformable neural radiance fields. *ICCV*, 2021a.
- Keunhong Park, Utkarsh Sinha, Peter Hedman, Jonathan T. Barron, Sofien Bouaziz, Dan B. Goldman, Ricardo Martin-Brualla, and Steven M. Seitz. Hypernerf: A higher-dimensional representation for topologically varying neural radiance fields. *CoRR*, abs/2106.13228, 2021b. URL <https://arxiv.org/abs/2106.13228>.
- Albert Pumarola, Enric Corona, Gerard Pons-Moll, and Francesc Moreno-Noguer. D-nerf: Neural radiance fields for dynamic scenes. *arXiv preprint arXiv:2011.13961*, 2020.
- Christian Reiser, Songyou Peng, Yiyi Liao, and Andreas Geiger. Kilonerf: Speeding up neural radiance fields with thousands of tiny mlps. *CoRR*, abs/2103.13744, 2021. URL <https://arxiv.org/abs/2103.13744>.
- Vincent Sitzmann, Michael Zollhöfer, and Gordon Wetzstein. Scene representation networks: Continuous 3d-structure-aware neural scene representations. In *Advances in Neural Information Processing Systems*, 2019.
- Cheng Sun, Min Sun, and Hwann-Tzong Chen. Direct voxel grid optimization: Super-fast convergence for radiance fields reconstruction. *CoRR*, abs/2111.11215, 2021. URL <https://arxiv.org/abs/2111.11215>.
- Panagiotis Symeonidis and Andreas Zioupos. *Matrix and Tensor Factorization Techniques for Recommender Systems*. SpringerBriefs in Computer Science. Springer, London, 2016. ISBN 978-3-319-41356-3. doi: 10.1007/978-3-319-41357-0.
- Jiaxiang Tang, Xiaokang Chen, Jingbo Wang, and Gang Zeng. Point scene understanding via disentangled instance mesh reconstruction, 2022a. URL <https://arxiv.org/abs/2203.16832>.
- Jiaxiang Tang, Xiaokang Chen, Jingbo Wang, and Gang Zeng. Compressible-composable nerf via rank-residual decomposition. *arXiv preprint arXiv:2205.14870*, 2022b.

- Edgar Tretschk, Ayush Tewari, Vladislav Golyanik, Michael Zollhöfer, Christoph Lassner, and Christian Theobalt. Non-rigid neural radiance fields: Reconstruction and novel view synthesis of a deforming scene from monocular video. *CoRR*, abs/2012.12247, 2020. URL <https://arxiv.org/abs/2012.12247>.
- Ledyard R. Tucker. Some mathematical notes on three-mode factor analysis. *Psychometrika*, 31(3): 279–311, Sep 1966. ISSN 1860-0980. doi: 10.1007/BF02289464. URL <https://doi.org/10.1007/BF02289464>.
- Zhou Wang, A.C. Bovik, H.R. Sheikh, and E.P. Simoncelli. Image quality assessment: from error visibility to structural similarity. *IEEE Transactions on Image Processing*, 13(4):600–612, 2004. doi: 10.1109/TIP.2003.819861.
- Jinmian Ye, Guangxi Li, Di Chen, Haiqin Yang, Shandian Zhe, and Zenglin Xu. Block-term tensor neural networks. *CoRR*, abs/2010.04963, 2020. URL <https://arxiv.org/abs/2010.04963>.
- Alex Yu, Sara Fridovich-Keil, Matthew Tancik, Qinhong Chen, Benjamin Recht, and Angjoo Kanazawa. Plenoxels: Radiance fields without neural networks. *CoRR*, abs/2112.05131, 2021a. URL <https://arxiv.org/abs/2112.05131>.
- Alex Yu, Ruilong Li, Matthew Tancik, Hao Li, Ren Ng, and Angjoo Kanazawa. Plenotrees for real-time rendering of neural radiance fields. *CoRR*, abs/2103.14024, 2021b. URL <https://arxiv.org/abs/2103.14024>.
- Richard Zhang, Phillip Isola, Alexei A. Efros, Eli Shechtman, and Oliver Wang. The unreasonable effectiveness of deep features as a perceptual metric. *CoRR*, abs/1801.03924, 2018. URL <http://arxiv.org/abs/1801.03924>.

A APPENDIX



Figure 7: Synthesized images of D-TensoRF-MM192 with different numbers of voxels.

Table 5: Per-scene quantitative evaluation on the extended Synthetic Nerf dataset provided by D-NeRF (Pumarola et al. (2020)).

Method	Hell Warrior			Mutant			Hook		
	PSNR \uparrow	SSIM \uparrow	LPIPS \downarrow	PSNR \uparrow	SSIM \uparrow	LPIPS \downarrow	PSNR \uparrow	SSIM \uparrow	LPIPS \downarrow
NeRF (Mildenhall et al. (2021))	13.52	0.81	0.25	20.31	0.91	0.09	16.65	0.84	0.19
DirectVoxGO (Sun et al. (2021))	13.52	0.75	0.25	19.45	0.89	0.12	16.16	0.80	0.21
Plenoxels (Yu et al. (2021a))	15.19	0.78	0.27	21.44	0.91	0.09	17.90	0.81	0.21
TensoRF-CP384 (Chen et al. (2022))	14.2	0.81	0.28	21.05	0.91	0.11	17.83	0.84	0.2
TensoRF-VM192 (Chen et al. (2022))	13.53	0.77	0.31	20.81	0.91	0.11	17.27	0.83	0.2
T-NeRF (Pumarola et al. (2020))	23.19	0.93	0.08	30.56	0.96	0.04	27.21	0.94	0.06
D-NeRF (Pumarola et al. (2020))	25.02	0.95	0.06	31.29	0.97	0.02	29.25	0.96	0.11
TiNeuVox-S (Fang et al. (2022))	27.00	0.95	0.09	31.09	0.96	0.05	29.30	0.95	0.07
TiNeuVox-B (Fang et al. (2022))	28.17	0.97	0.07	33.61	0.98	0.03	31.45	0.97	0.05
D-TensoRF-CP768	23.65	0.93	0.07	32.35	0.97	0.02	27.73	0.95	0.04
D-TensoRF-MM192	22.59	0.92	0.08	32.63	0.97	0.02	27.54	0.95	0.04
Method	Bouncing Balls			Lego			T-Rex		
	PSNR \uparrow	SSIM \uparrow	LPIPS \downarrow	PSNR \uparrow	SSIM \uparrow	LPIPS \downarrow	PSNR \uparrow	SSIM \uparrow	LPIPS \downarrow
NeRF (Mildenhall et al. (2021))	20.26	0.91	0.20	20.30	0.79	0.23	24.49	0.93	0.13
DirectVoxGO (Mildenhall et al. (2021))	20.20	0.87	0.22	21.13	0.90	0.10	23.27	0.92	0.09
Plenoxels (Yu et al. (2021a))	21.30	0.89	0.18	21.97	0.90	0.11	25.18	0.93	0.08
TensoRF-CP384 (Chen et al. (2022))	21.03	0.9	0.17	21.61	0.91	0.09	25.25	0.94	0.08
TensoRF-VM192 (Chen et al. (2022))	20.89	0.9	0.16	21.44	0.9	0.1	25.1	0.94	0.08
T-NeRF (Pumarola et al. (2020))	37.81	0.98	0.12	23.82	0.90	0.15	30.19	0.96	0.13
D-NeRF (Pumarola et al. (2020))	38.93	0.98	0.10	21.64	0.83	0.16	31.75	0.97	0.03
TiNeuVox-S (Fang et al. (2022))	39.05	0.99	0.06	24.35	0.88	0.13	29.95	0.96	0.06
TiNeuVox-B (Fang et al. (2022))	40.73	0.99	0.04	25.02	0.92	0.07	32.70	0.98	0.03
D-TensoRF-CP768	41.52	0.99	0.005	25.38	0.94	0.03	31.23	0.97	0.03
D-TensoRF-MM192	39.15	0.99	0.01	25.30	0.94	0.03	30.18	0.97	0.03
Method	Stand Up			Jumping Jacks					
	PSNR \uparrow	SSIM \uparrow	LPIPS \downarrow	PSNR \uparrow	SSIM \uparrow	LPIPS \downarrow			
NeRF (Mildenhall et al. (2021))	18.19	0.89	0.14	18.28	0.88	0.23			
DirectVoxGO (Mildenhall et al. (2021))	17.58	0.86	0.16	17.80	0.84	0.20			
Plenoxels (Yu et al. (2021a))	18.76	0.87	0.15	20.18	0.86	0.19			
TensoRF-CP384 (Chen et al. (2022))	18.29	0.88	0.18	19.29	0.88	0.23			
TensoRF-VM192 (Chen et al. (2022))	18.96	0.89	0.15	19.41	0.87	0.24			
T-NeRF (Pumarola et al. (2020))	31.24	0.97	0.02	32.01	0.97	0.03			
D-NeRF (Pumarola et al. (2020))	32.79	0.98	0.02	32.80	0.98	0.03			
TiNeuVox-S (Fang et al. (2022))	32.89	0.98	0.03	32.33	0.97	0.04			
TiNeuVox-B (Fang et al. (2022))	35.43	0.99	0.03	34.23	0.98	0.03			
D-TensoRF-CP768	32.59	0.98	0.02	31.01	0.97	0.03			
D-TensoRF-MM192	32.00	0.97	0.02	30.13	0.97	0.04			



Figure 8: Rendering results of D-TensoRF-CP. Images of each scene are synthesized under different time conditions with the same viewing direction. The eight scenes are provided by D-NeRF (Pumarola et al. (2020)).



Figure 9: Rendering results of D-TensorRF-MM. Images of each scene are synthesized under different time conditions with the same viewing direction. The eight scenes are provided by D-NeRF (Pumarola et al. (2020)).



Figure 10: Rendering results of D-TensorRF-CP. Images of each scene are synthesized under different viewing directions with the same time condition. The eight scenes are provided by D-NeRF (Pumarola et al. (2020)).



Figure 11: Rendering results of D-TensoRF-MM. Images of each scene are synthesized under different viewing directions with the same time condition. The eight scenes are provided by D-NeRF (Pumarola et al. (2020)).